International Journal of Civil Engineering (2021) 19:823–836
https://doi.org/10.1007/s40999-021-00608-w

RESEARCH PAPER

Three-dimensional Nonlinear Finite Element Analysis for Load-Carrying Capacity Prediction of a Railway Arch Bridge

Mahdi Yazdani[1]

Received: 10 March 2020 / Revised: 16 December 2020 / Accepted: 31 January 2021 / Published online: 9 March 2021

Abstract
Calculation of load-carrying capacity of old railway masonry arch bridges as crucial infrastructures is one of the vital issues in the railway industry. The field test of the 2PL20 bridge reveals important properties such as the initial stiffness and cracking pattern, but the ultimate capacity of the bridge under static loading was not achieved due to the field limitations. Therefore, the present study aims to predict the total nonlinear response of the 2PL20 bridge up to the failure status. All the geometrical characteristics of the 2PL20 bridge are modeled precisely and the failure state is predicted using the three-dimensional nonlinear finite element analysis. Moreover, to determine the load-carrying capacity of the 2PL20 bridge, the behavior of materials is regarded nonlinearly in which the Williams and Warnke and the Drucker-Prager failure criteria are taken into account for concrete and soil materials, respectively. To obtain precise results of ultimate capacity of the 2PL20 bridge under field test, the vertical and horizontal displacements of the crown on the northern span are chosen as the calibration criterion and, consequently, the vertical and horizontal load-deformation curves are verified based on the field test results. The obtained results indicate that the load-carrying capacity of the 2PL20 bridge equals 8880 kN under the static field test. Finally, the calculated safety factor is equal to 3.2 and increasing axial load up to 35-ton is admissible based on UIC 776-1 for a 25-ton axial load.

Keywords Masonry arch bridges · Railway bridges · Three-dimensional finite element simulation · Nonlinear static analysis · Load-carrying capacity · Safety assessment

1 Introduction

Assessment of old masonry arch bridges is an important issue for engineers and researchers. While the structural parts require an accurate modelling, the complicated behavior of such structures leads to field load testing. The structural behavior and load-carrying capacity of the masonry arch bridges have been studied frequently by many ways from the past to the present. Totally, these approaches are divided into three main groups: empirical, analytical, and numerical methods. In all the three groups, the experimental test is an essential part of the study. The first one, proposed by the British defense research unit in 1946, led to the semi-empirical method, which was named Military Engineering Experimental Establishment (MEXE) [1]. This method was developed to quick assessment of masonry arch bridges. The MEXE is based on the classic theoretical approaches to study the stability of masonry arches. This method has been extended in recent years and reported in Ref. [2]. The most important analytical methods are the mechanism and limit analysis methods, the former was extracted by Heyman's works as an equilibrium-based model and subsequently the latter was developed based on Heyman's works [3]. As a frequently used method, the limit analysis is currently implemented in the Ring limit state software. Then, the numerical methods are used as a powerful alternative approach with no limitations. The most important approaches used as a numerical method to assess the masonry arch bridges are finite element and discrete-element methods [4]. These two methods are used in macro-modeling [5], meso-modeling [6], and micro-modeling approaches [7] for one-dimensional [8], two-

✉ Mahdi Yazdani
m-yazdani@araku.ac.ir

[1] Department of Civil Engineering, Faculty of Engineering, Arak University, P.O. Box 38158–879, Arak, Iran

dimensional [9], and three-dimensional [10] modeling of masonry arch bridges.

The finite element analysis of masonry arches was first conducted in the 1980′s by the use of one-dimensional modeling (curved and cone beam elements) [11]. Subsequently, the finite element method has been widely used for modeling masonry arch bridges [12, 13]. In 2002, for example, the service load of masonry arch bridges was evaluated by the three-dimensional nonlinear finite element method in mesoscale approach [14]. In 2012, the micro-modeling technique was used by finite element approach to predict the ultimate capacity of two stone arch bridges under static loads [15]. To overcome the finite element method restriction, the discrete element method as an alternative has also been widely used in the last decades in micro-scale approach to determine load-carrying capacity of masonry arch bridges [16, 17]. For example, the effect of construction method on the load-bearing capacity of a single span skew masonry arch using the discrete element method has been taken into account in recent years [18]. In addition to the numerical simulations, extensive researches were concentrated on the experimental works [19, 20]. For example, many field tests were performed on the masonry arch bridges to obtain service capacity and ultimate collapse load in the 1990′s [21].

Moreover, various works have been conducted about two-dimensional and three-dimensional numerical simulations in linear, nonlinear, plastic, and fracture mechanics conditions to compute the failure status of masonry arch bridges, for which references [22, 23] could be mentioned for more information. In addition to the mentioned researches that accomplished to evaluate the ultimate capacity of masonry arch bridges under static conditions, more works have been performed on dynamic analyses [24–26] and seismic assessment analyses of these types of structures [27–29].

Based on material construction, masonry arch bridges may be divided into three classes: brickwork arch bridges, stone arch bridges, and plain concrete arch bridges. While various numerical and experimental studies have frequently been reported on brickwork and stone arch bridges, a few field test studies have been conducted on plain concrete arch bridges [5, 19]. This study, therefore, aims to predict the load-carrying capacity of a plain concrete arch bridge under field loading and UIC 776–1 axial loading conditions by a comprehensive three-dimensional nonlinear finite element model.

2 Field Test on Considered Railway Arch Bridge

In this section the summary of field test of a masonry arch bridge is presented. For more information about the field test please refer to reference [5].

2.1 Discription of the Bridge

The considered bridge which has been built more than 80 years ago is placed in kilometer 23 of Tehran-Qom old railway and consists of two identical 20-m spans. For further simplification the considered bridge is named 2PL20 bridge. Reinforcement has not been used and all structural parts 2PL20 bridge including the arch, spandrel wall, abutment, wing wall, pier and foundation are plain concrete constructions. Thin layer of concrete has been used as a material to level out the surface above the arches. The structure suffers 10–30 mm initial cracks in the crown and in the middle springing of both arches which the width of the cracks at the intrados varies in depth and developed throughout the whole section of the arch. Other environmental damage has not been found in the 2PL20 bridge. Geometric properties of the 2PL20 bridge are shown in Fig. 1 and summarized in Table 1. To evaluate the quality of the concrete, mechanical properties of materials have been determined by cylindrical core test and represented in Table 2.

2.2 Results of Static Loading

To gain the ultimate capacity of 2PL20 bridge, load test carried out just on the northern span, statically using 40 kN weights. Figure 2 describes the static loading performed on the 2PL20 bridge. As it is shown, the load increases gradually by applying an incremental load of 240 kN. In this experimental study the variation of the vertical displacement and crack opening of the crown have been recorded and displayed in Fig. 3.

Field test observations demonstrated that new micro-cracks were appeared before starting nonlinear zone around the initial cracks in the springings and the crown. Although the initial cracks became wider. At a load level of around 3500 kN, the micro-cracks became detectable and through the increase of load, they turned into wider and deeper cracks. However, the slope of the vertical and horizontal load–displacement curves has remained almost constant up to 6240 kN which is illustrated in Fig. 3.

Large deformations begin in 6240 kN load, and the structural stiffness decrease remarkably. Loading had been continued up to 7280 kN, but due to safety consideration and field limitation, applying more loads was impossible

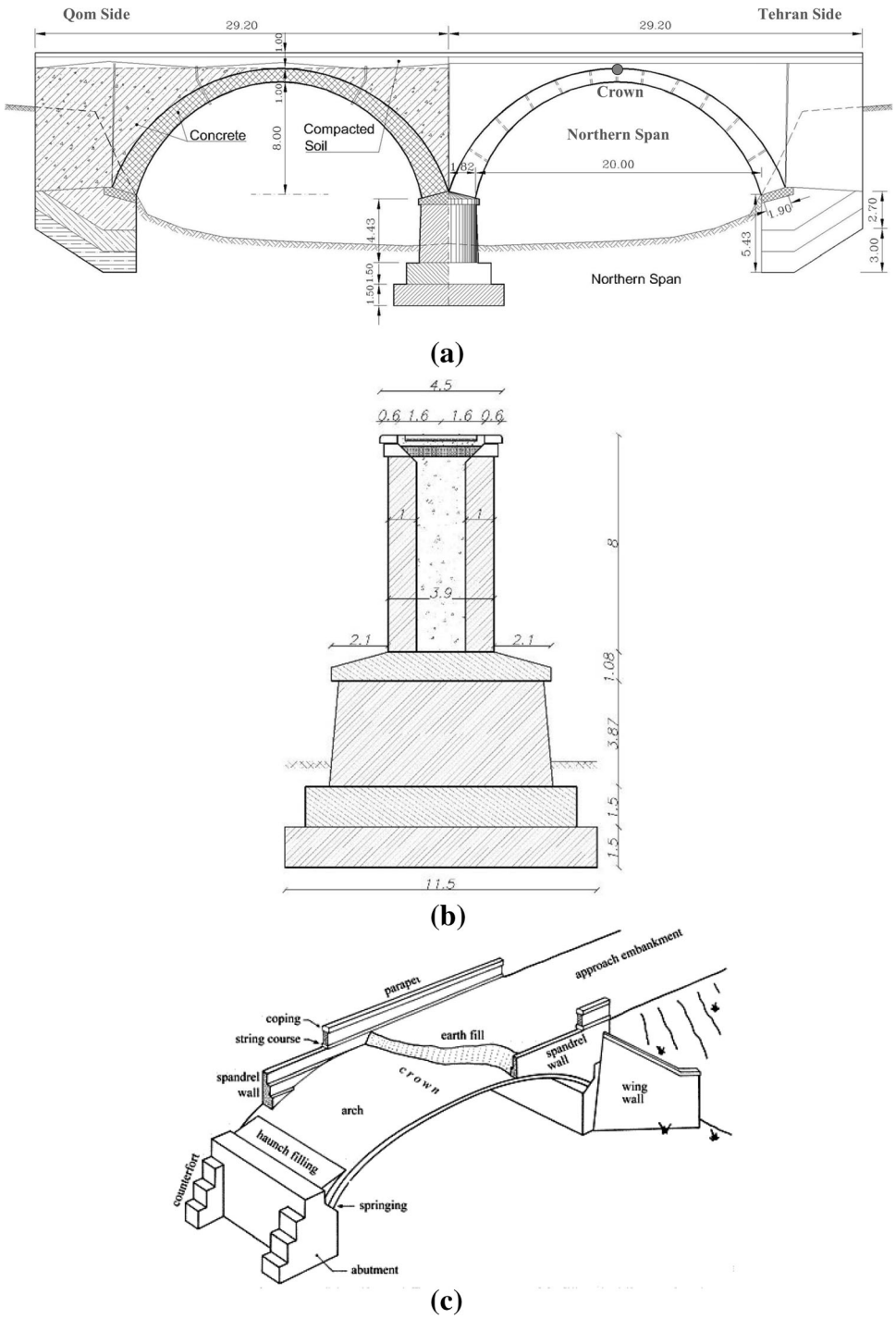

Fig. 1 Geometric characteristics of the 2PL20 bridge (units are in meter). **a** longitudinal section, (**b**) transversal section and (**c**) structural parts of Plain concrete arch bridges

and the test had stopped and did not continued until failure of the structure. In addition, due to intensive damage of heavy loading process, the bridge went out the service. However, the load applied in the field test is more than the service load of the current railway network, the load-carrying capacity of the 2PL20 bridge remains as a query, which determining it may be a vital step to recognize the nonlinear behavior of the plain concrete arch bridges. In the last stage of static loading (7280 kN), the cracking pattern does not change, so the cracks which appeared almost in the northern span and near the springings are named second cracks. After appearing the second cracks, it

Table 1 Geometric characteristics of the 2PL20 bridge

Bridge	2PL20
Total length	58.4 m
Width	4.4 m
Arches number	2
Piers	
Width	3.9 m
Length	3.6 m
Height	4.43 m
Arch	
Shape of arch	Segment of circle
Span	20 m
Rise at span	8 m
Vault thickness at the springing	1.9 m
Vault thickness at the crown	1.1 m
Spandrel walls	
Thickness	1 m

Table 2 Mechanical features of concrete based on tests of cylindrical cores

Material	Compressive strength (MPa)	Modulus of elasticity (GPa)	Density of concrete (kg/m^3)
Concrete-fill	17.6	20.2	2300
Arch	17.3	17.0	2280
Pier	27.9	37.3	2350

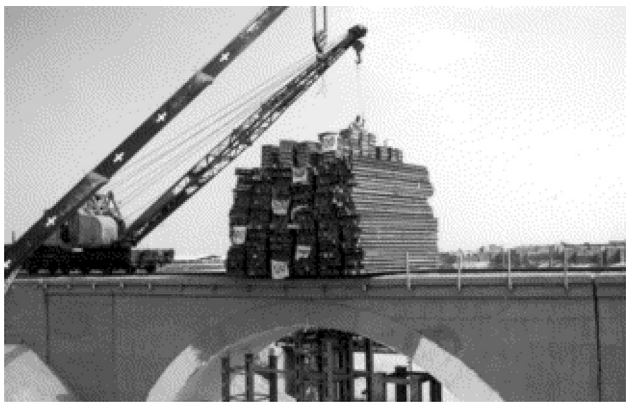

Fig. 2 Static loading of 2PL20 bridge

seems that the crack propagation patterns remain constant and does not reform in the post-yield state of the 2PL20 bridge. However, the depth and width of the both initial and second cracks increase with the loading process. The initial and second cracks are depicted in Fig. 4 in final stage of field test.

3 Three-Dimensional Finite Element Analysis

The actual behaviour of masonry arch bridges depends on the boundary conditions, material properties, changing features in sections, sliding between filling-materials and the arch, fatigue effects, the location and size of the cracks, environmental damage, discontinuities, and connectivity. Practically, considering all these parameters in simulations seems to be impossible and lead to high computational effort for these massive structures. Therefore, some of these parameters should be implemented indirectly in the numerical method (see Refs. [28, 30, 31]).

In this study, a comprehensive finite element model is established using the ANSYS FEM package. This program can be used for linear, nonlinear, static, and dynamic analysis of structures. Thus, different parts of the 2PL20 bridge, including the arches, the abutments, the spandrel walls, the wing walls, the piers, the foundation, and the filler materials, are modelled precisely by means of a macro-modelling, as depicted in Fig. 5. The soil was simulated in limited dimensions due to the complex and unknown boundary conditions of the bridge, on the one hand, and to incorporate side effects such as soil settlement, on the order hand [6]. Thus, the modelled soil allowed for properly defining the boundary conditions of the bridge. It should be noted that it was not required to model the soil in infinite dimensions, since the structure applied static loading to the soil [28]. According to the dominant behaviour of plain concrete arch bridges, macro-modelling and 3D eight-node solid isoperimetric elements (24 translation degrees of freedom for each element) are used to establish the primary finite element model (Fig. 6). Moreover, old unreinforced arch bridges typically undergo cracking after construction due to their weights and service loads in the crown or springings, being referred to as cracked structures. Therefore, the existing initial cracks are considered as void spaces in the finite element model to take account of the actual conditions of the bridge based on observation measurement. In addition, it can be noted that the initial cracks are modelled with the aim of assigning defects and pre-stress effects to the numerical model before starting the analysis. For this purpose, all cracks are considered as void spaces to consider decreasing in the strength of the 2PL20 bridge. Accordingly, the features mentioned by fracture mechanics theory as the stress intensity factor are not used for initial cracks. According to the supposed assumptions, Fig. 6 represents the details of the final finite element model.

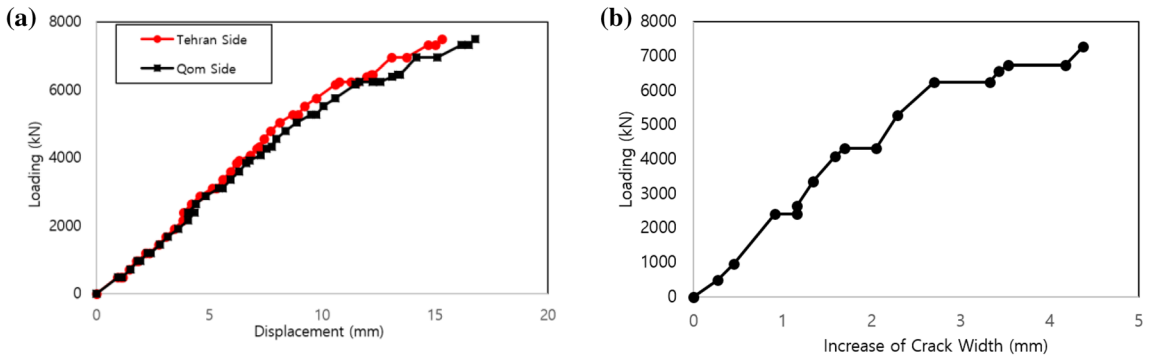

Fig. 3 Displacement of the 2PL20 bridge, at the crown, under static loading: (**a**) variation of vertical direction and (**b**) variation of crack width (horizontal direction)

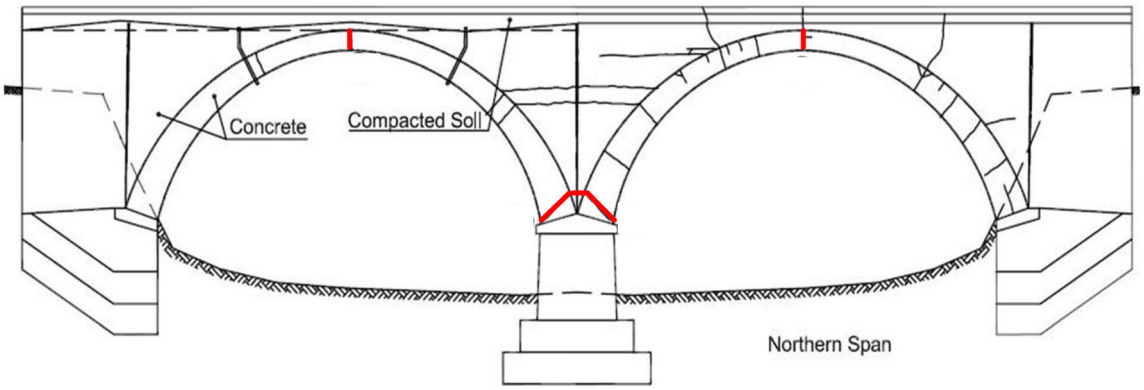

Fig. 4 Crack pattern at final stage of static loading (field test). Cracks represented by red existed before the test (initial cracks)

After implementing the geometric features of the finite element method in the primary numerical model, material properties are defined in the finite element model based on the cylindrical core test results. In this simulation, material behavior is considered to act nonlinearly and fracture mechanic theory is taken into account to calculate the structural damage. In computational fracture mechanics, two approaches are generally adopted to analyze cracked solids and structures, including (i) geometrical modeling [32, 33] and (ii) non-geometrical modeling [34]. The former models the crack geometry, while the latter non-geometrically incorporates the effects of defects. The geometrical approach involves two sub-approach; the first ones is related to traditional finite element method in which the crack growth path is dependent on the geometry of elements. The second sub-approach, on the other hand, includes adaptive finite element method and utilizes the idea of re-meshing to implement the crack propagation. Thus, the crack growth path is independent of the element geometry. The non-geometrical approach is further divided into two sub-approaches. The first sub-approach includes behavior equation-based methods. This sub-approach does not model cracks but treats the area around the cracks as a weak region that can be incorporated in the form of reduced strength or reduced stiffness. Furthermore, it may use the elimination of elements; instead of weakening the intended area, element elimination is applied to exclude the cracked region. The smeared cracking method is among the most used techniques of the first non-geometrical sub-approach type, which has been of great interest to researchers. The second non-geometrical sub-approach, on the other hand, includes kinematic methods that utilize enrichment methods. It changes formulation, unlike the first non-geometrical sub-approach. Thus, the second non-geometrical sub-approach enjoys the advantages of geometrical modeling. The extended finite element method is a technique of the second non-geometrical sub-approach [35].

Based on Fig. 7, *William and Warnke* and *Drucker-Prager* failures are implemented for the tri-axial behavior based on a constitutive model for concrete and soil material, respectively. The criterion for the failure of concrete due to a multi-axial stress state can be expressed in the following form:

$$\frac{F}{f_c'} - S \geq 0 \tag{1}$$

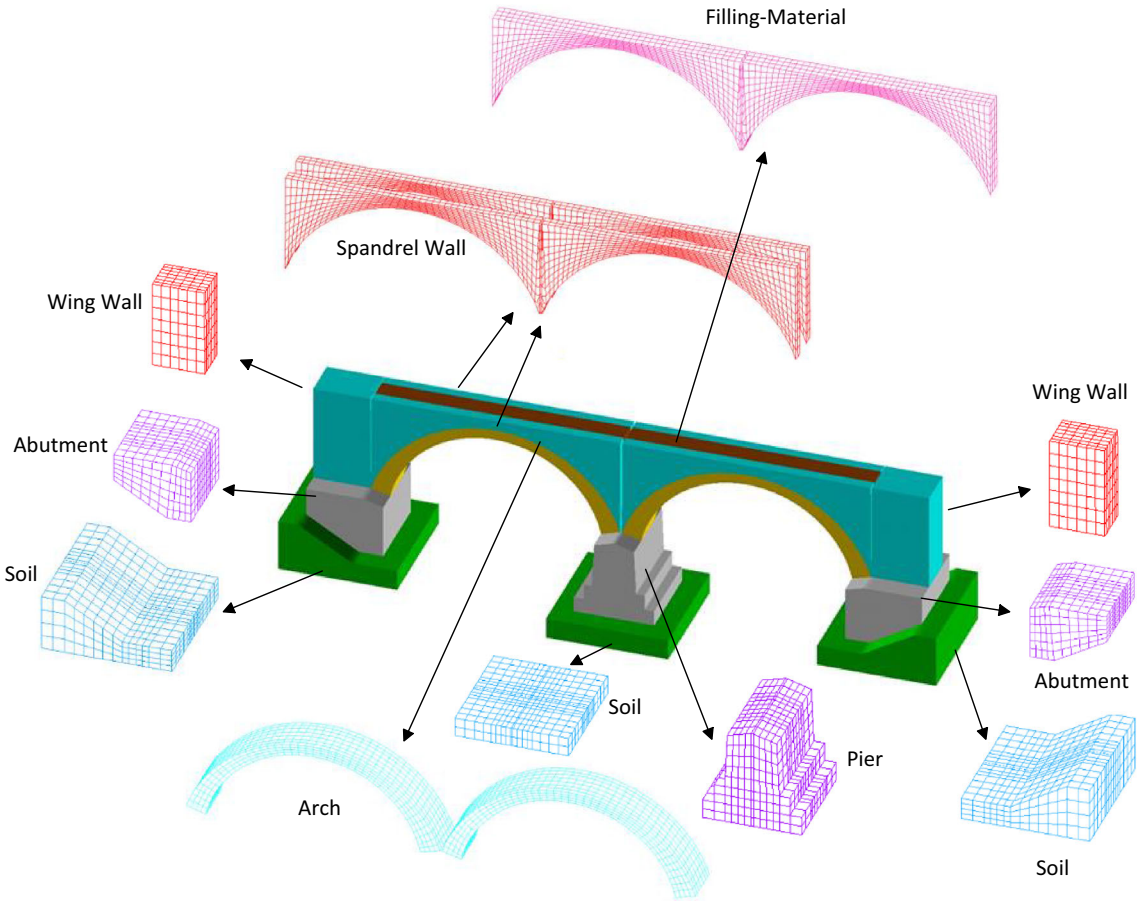

Fig. 5 Modeling different parts of the 2PL20 bridge by the ANSYS FEM package

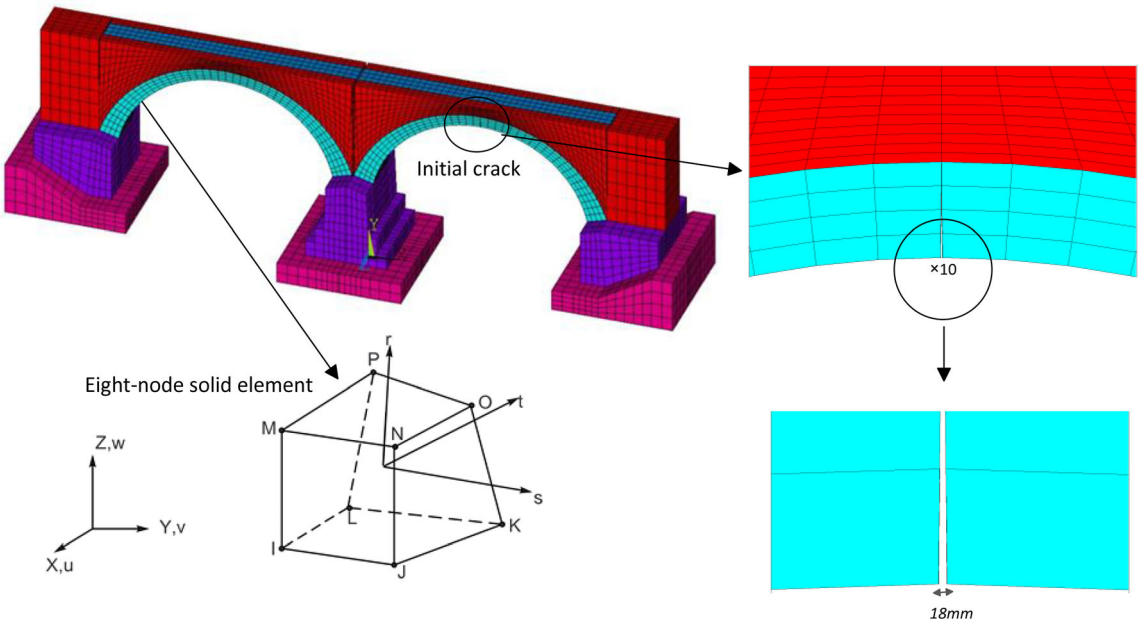

Fig. 6 Final three-dimensional finite element model of the 2PL20 bridge with eight-node elements (with 24 degrees of freedom) and initial cracks in the crown of the arches

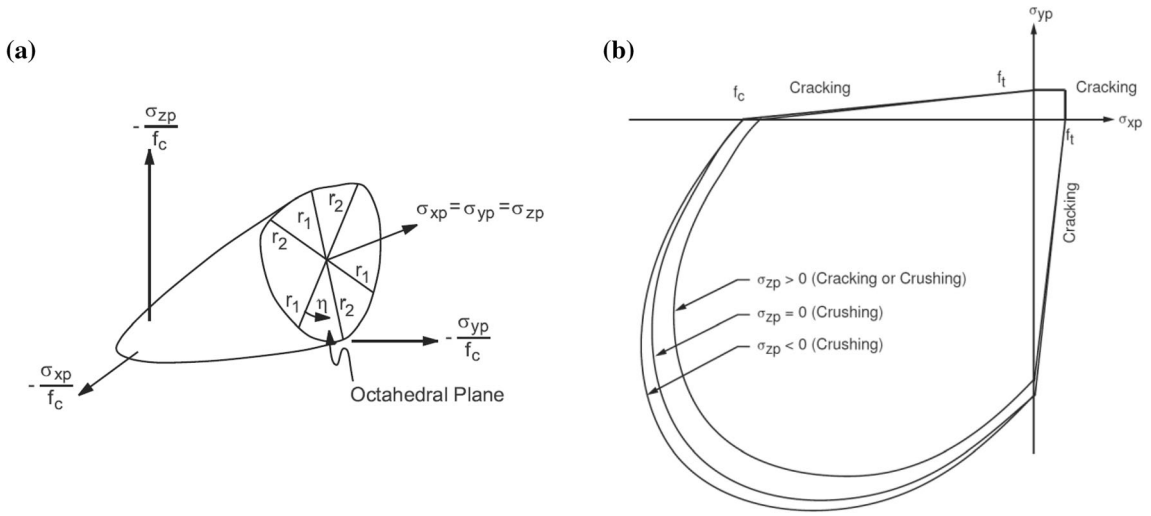

Fig. 7 William and Warnke failure criterion: (**a**) three-dimensional surface in principal stress and (**b**) failure surface in principal stress space with nearby biaxial stress

where F indicates a function of the principal stress state (σ_{xp}, σ_{yp}, σ_{zp}) in which σ_{xp}, σ_{yp} and σ_{zp} describe principal stresses in principal directions. S stands for failure surface expressed in terms of principal stresses and seven input parameters are needed to define as [36]:

- Ultimate uniaxial tensile strength (f_t)
- Ultimate uniaxial compressive strength ($f_c^{'}$)
- Ultimate biaxial compressive strength (f_{cb})
- Ambient hydrostatic stress state (σ_h)
- Ultimate compressive strength for a state of biaxial compression superimposed on the hydrostatic stress state (f_1)
- Ultimate compressive strength for a state of uniaxial compression superimposed on the hydrostatic stress state (f_2)
- Shear transfer coefficients (β_t and β_c)

However, the failure surface can be specified with a minimum of two constants, f_t and $f_c^{'}$. The following three constants are equal to the defaults of Willam and Warnke

$$f_{cb} = 1.2f_c^{'} \tag{2}$$

$$f_1 = 1.45f_c^{'} \tag{3}$$

$$f_2 = 1.725f_c^{'} \tag{4}$$

However, these default values are valid only for stress states under the following condition

$$|\sigma_h| \leq \sqrt{3}f_c \tag{5}$$

Since the compressive strength of concrete was derived from the cylindrical core test, other failure parameters of these models may be extracted directly as mentioned above. Additionally, the maximum tensile strength of concrete (f_t) is assumed as $\left(f_t = 0.56\sqrt{f_c^{'}}\right)$ in which it is proposed by ACI 318–11 [37]. In addition, β_t is defined that denotes a shear strength reduction factor for those subsequent loads that induce sliding across the crack face. If the crack is closed, then all the compressive stress normal to the crack plane are transferred across the crack, thereby defining β_c. Besides, $\beta_t = 0.25$ and $\beta_c = 0.8$ are considered in this study [14].

It is worthwhile to mention that the constitutive model was supposed based on a smeared crack model in fracture mechanics theory to allow the formation of cracks perpendicular to the direction of principal stresses that exceed the tensile strength of the concrete. This model is also considered both cracking in tension zone and crushing in compressive zone. Cracking or crushing of an element is started when one of the principal stresses of an element at integration points exceed the tensile or compressive strength of the domain. Cracked or crushed zones, as opposed to discrete cracks, are then formed perpendicular to the relevant principal stress direction with stresses being redistributed locally; hence, the element is nonlinear and needs an iterative solver. In the numerical procedures, the formation of crack is gained by the adaptation of the stress–strain relationship of the element to present a plane of weakness in the requisite principal stress direction. The amount of shear transfer across a crack can vary between full shear transfer and no shear transfer at a cracked section. The crushing algorithm is similar to a plasticity law in that when a section has crushed, further application of load in that direction progresses the increasing strain at constant stress (see Fig. 7). Following the formation of an initial crack, stresses tangential to the crack face may cause a second or third crack to develop at integration point [14].

In addition, the behavior of the concrete material is simulated by the use of a solid element that can have its stiffness adapted by the expansion of cracks and crushing. This criterion is frequently used to calculate the failures that occurred in concrete structures [38].

To employ the Drucker–Prager yield criterion, the following three parameters are demanded as input data:

- cohesion (c)
- angle of internal friction (φ)
- angle of dilation (ψ)

These three parameters are extracted directly from the f_t and $f_c^{'}$. In the second step of the simulation procedure, uncertain parameters such as boundary conditions, mechanical properties of the filler material, and the soil underneath the foundation are chosen as variable parameters for calibrating the finite element model. By calibrating the variable parameters, the finite element model can designate the actual behavior of the bridge. In addition to the calibration procedure, sensitive analysis is taken into account to subsequently determine variable parameters. To get better sense of the precise finite element model with low computational cost, the calibration procedure and sensitive analysis are done simultaneously. For this reason, by selecting the size of elements between 0.1 and 1.2 m, totally 18,819 eight-node solid elements with 63,096 degrees of freedom are used for the 2PL20 bridge model (see Figs. 5 and 6). Finally, final properties of the materials are displayed in Table 3.

4 Numerical Results

To validate the finite element model of the 2PL20 bridge, the vertical displacement and the crack opening of the crown in the northern span are compared with the field test results. Figure 8 presents to get a better sense of the accuracy of the finite element model. As it is clear, the finite element results have a good compatibility with the experimental results in both small and large deformation stages. It is worthwhile to mention that the calibration parameters are altered in model updating process until the experimental and the numerical results converge together.

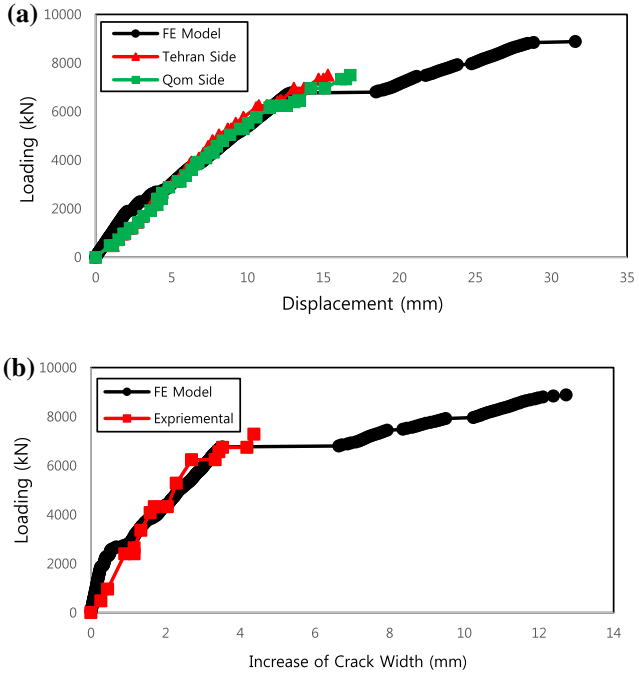

Fig. 8 Comparison of variation displacement of the 2PL20 bridge for the northern span at the crown: (**a**) vertical displacement and (**b**) crack width variation

In the nonlinear static analysis, element matrices are computed by the Gaussian numerical integration. In addition, the nonlinear static analysis is solved by the Newton–

Table 3 Final mechanical features of materials

Material behavior	Material law	Mechanical features	Soil	Filler material	Arch	Pier, abutment, foundation	Wing wall, spandrel wall
Linear	Hook	γ(ton/m^3)	1.8	2	2.28	2.35	2.3
		E(GPa)	0.1	0.5	17	37.3	20.2
		v	0.33	0.3	0.21	0.17	0.2
Nonlinear	Drucker–Prager	c(MPa)	0.4	0.5	–	–	–
		φ°	30	30	–	–	–
		ψ°	2	2	–	–	–
	Willam and Warnke	$f_c^{'}$(MPa)	–	–	17.3	27.9	17.6
		f_t(MPa)	–	–	2.33	2.96	2.35
		f_{cb}(MPa)	–	–	20.76	33.48	21.12
		f_1(MPa)	–	–	25.08	40.45	25.52
		f_2(MPa)	–	–	29.84	48.13	30.36

Raphson algorithm with a load increment of dF = 40 kN. Finally, by defining the displacement as convergence criterion, the failure load of the 2PL20 bridge is determined equal to 8880 kN in a total of 222 steps of analysis. Displacement field and progress of damaged zone of the 2PL20 bridge in the failure stage (8880 kN load) are depicted in Figs. 9 and 10. As shown in Fig. 10, the maximum displacement of the 2PL20 bridge occurs in the crown due to the existing initial cracks. By comparing Figs. 4 and 10, it may also be concluded that the damaged zones or cracking pattern of the 2PL20 bridge, determined by finite element analysis, have adequate compatibility with the field results. Although Fig. 4 is not presented for damaged zone of the 2PL20 bridge in the ultimate capacity, it may be concluded that the cracking pattern does not change after starting post-yield behavior and the revealed cracks only become much wider and deeper.

Based on the cracking pattern depicted in Fig. 10, it may be derived that the location of damaged zones is related to the plastic hinges (or nonlinear zones). The figure also shows that three plastics hinges have formed in the northern span of the 2PL20 bridge, which include the crown and each of the springings. To better understand the formation of the three plastic hinges, two fundamental concepts are presented based on Fig. 11. The variation of failure principle stress criterion of crack-tip (crown) in the northern span of the 2PL20 bridge versus loading is shown in Fig. 11a. It is observed that the failure principle stress criterion had jumping in three stages; therefore, it may be concluded that severe changes in these three stages are exactly the plastic zones (hinges) in the 2PL20 bridge (see Fig. 11b). Despite this conceptual way, three plastic hinges may be represented by the variation of curvature of load-deformation slope (see Fig. 11c). As depicted in Fig. 11d, this way proves the formation of three plastic hinges. By comparing Fig. 11b, d, it can be concluded that the moments of the first and third plastic hinges are similar but the second one is different.

Most of researchers believe that four plastic hinge formation may cause failure in the masonry arch bridges, and failure was also reported by 3 and 5 plastic hinges in some cases [21]. However, they assert that plastic hinge formation is dependent on geometric properties of the bridge part and the distance of loading to the crown. The failure mechanism of the 2PL20 bridge, which does not occur based on four plastic hinge formation (common failure mechanism in arches), is due to the similar mechanical properties of the spandrel walls and the arch (see Table 2), and complicated geometry of the bridge. Hence, it may be concluded that the behavior of the 2PL20 bridge, which is not identical to the common masonry arch bridges and the failure mechanism of this bridge, is different from other masonry bridges (in masonry arch bridges, the mechanical properties of spandrel walls and fill materials are usually more less than arches) [5, 21]. As a result, it may be declared that the pattern obtained for the plastic hinge formation and the displacement-load curve may be accurate and acceptable. Likewise, the estimated load-carrying capacity of the 2PL20 bridge is about 8880 kN and is completely reliable.

5 Saftey Assessment

Determination of load-carrying capacity of masonry arch bridges has been considered in many studies. For example, the geometric and mechanical properties of 50 masonry arch bridges of Italian railway network were collected to assess the safety of the bridges [39]. The results indicated that the safety factor of considered bridges was from 2 up to 30 based on UIC 776-1 loading. In addition to geometric and mechanical properties, the real safety factor may be affected by abundant factors, such as environmental deterioration and fatigue. For the latter, experimental observations demonstrated that repeated cyclic loading over 50% of the final static strength might induce fatigue failure [40]. For more information about safety assessment of masonry bridges, the reader is referred to [41]. The results of finite element simulation under static field test and UIC 776-1 train live loading for calculation of safety factor are presented in this section.

5.1 Results of Static Field Loading

As shown in Sect. 4, the load-carrying capacity of the 2PL20 bridge is determind according to the Fig. 8. Therefore, if λ is defined by the ratio of collapse load (CL) and plastic hinges (PH) as

$$\lambda = \frac{CL}{PH_i} \tag{6}$$

where $i = 1,2,3$; λ is computed as $\lambda_1 = (8880/2600) = 3.415$, $\lambda_2 = (8880/5160) = 1.721$, and $\lambda_3 = (8880/8840) = 1.005$. Then, the load factor for a possible collapse mechanism is denoted as

$$\mathrm{LF}_{jk} = \frac{\lambda_j}{\lambda_k} \tag{7}$$

where $j,k = 1,2,3$ for $j<k$. Consequently, LF is determined as $\mathrm{LF}_{12} = (3.415/1.721) = 1.984$, $\mathrm{LF}_{13} = (3.415/1.005) = 3.980$, and $\mathrm{LF}_{23} = (1.721/1.005) = 1.712$. Another important parameter in the assessment of nonlinear behavior of the masonry arch bridges is ductility factor (DF). Based on the Fig. 9, it may be rather assumed that the 2PL20 bridge behavior is linear up to the displacement of 12.87 mm (LS), and the nonlinear behavior starts from this point, continues

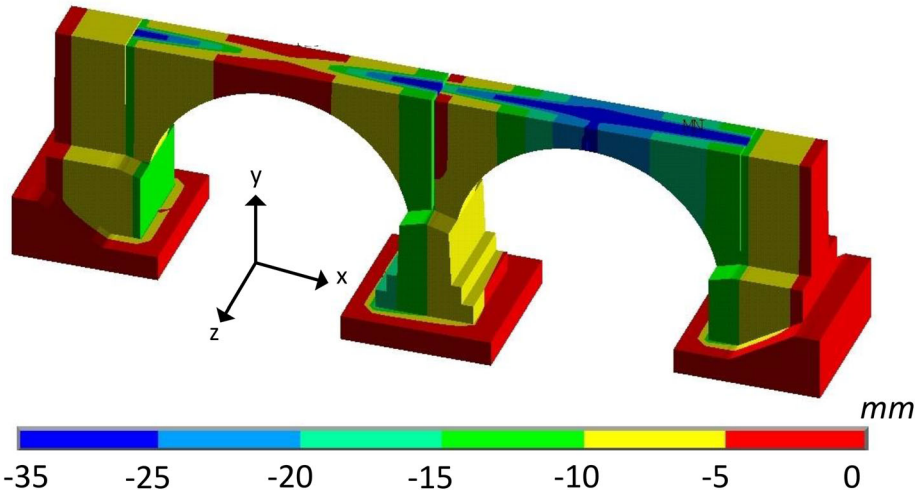

Fig. 9 Vertical deformation of the 2PL20 bridge in the failure state (8880 kN)

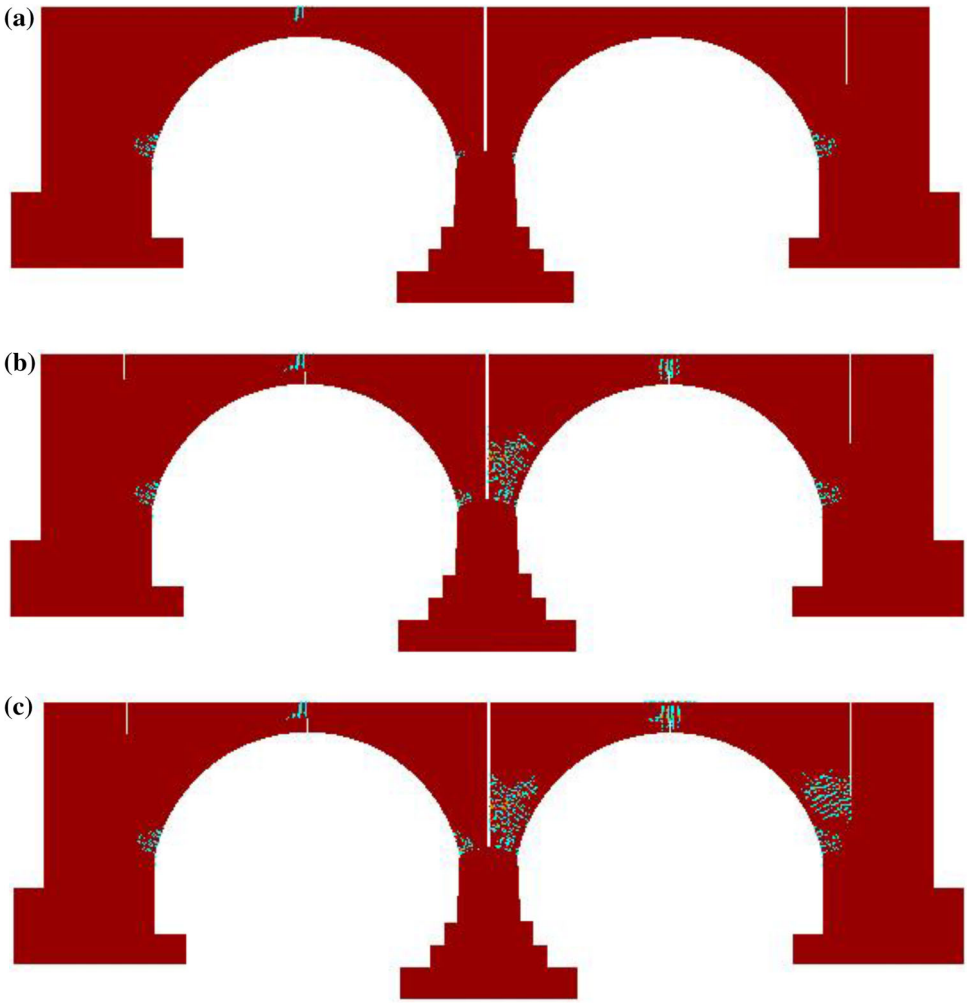

Fig. 10 Damaged zone progress in different stages. **a** Cracked media in 3000 kN load, **b** cracked media in 7280 kN Load, and **c** final cracked media in collapse state (8880 kN load)

up to the large deformations, and collapse occurs in 32.66 mm displacement (*US*). Based on the considered assumptions, the ductility factor may be derived as

$$\mathrm{DF} = \frac{\mathrm{US}}{\mathrm{LS}} \tag{8}$$

Thus, the ductility factor of the 2PL20 bridge is computed as $\mathrm{DF} = (32.662/13.206) = 2.473$. Regardless of the fact that the reinforcement was not used in the 2PL20 bridge, the structure benefits from an appropriate ductility, and it could be emphasized that the 2PL20 bridge has an appropriate nonlinear behavior.

5.2 Safety Factor

In addition to the static loading of field test, the UIC 776-1 code was used for the assessment of the 2PL20 bridge under 25-ton axial service live train load [42]. As depicted in Fig. 12, the service load in the UIC 776-1 code for the railway bridges was 4 concentrated loads of 250 kN with a distance of 1.6 m and two distributed loads of 80 kN/m with a distance of 0.8 m from the concentrated loads. Subsequently, to obtain the factor of safety, the ratio of the applied load to the service load of the UIC 776-1 is augmented until failure happens in the bridge. Results indicate that the residual capacity of the bridge under train live loads is much higher than the service load. For this reason, the results discussed herein are based on the most critical states reported in [39]. Since it constrains the upward deflection of the arches adjacent to the loaded span and prevents the development of the collapse mechanism, which leads in turn to a higher load carrying capacity, the distributed load is not included in the critical load pattern (different for deck bridges). Therefore, the design exercise load (DEL) value is 1000 kN $(4 \times 25\text{ton})$ per track line running on the bridge [39]. Hence, the factor of safety (FS) may be computed by the ratio of CL and DEL as

$$\mathrm{FS} = \frac{\mathrm{CL}}{\mathrm{DEL}} \tag{9}$$

According to the UK highway agency, the safe capacity of masonry arch bridges is 50% of ultimate load-carrying capacity [43]. Accordingly, the FS of the 2PL20 bridge is figured as $\mathrm{FS} = 0.5 \times (6400/1000) = 3.200$. The limit state as an analytical approach is used to validate the obtained safety factor. This method is implemented in the Ring software and recommend by the UK highway agency to calculate the ultimate load capacity of masonry arch bridges. Based on Fig. 13, the collapse load and mechanism state of the 2L20 bridge are determined in critical

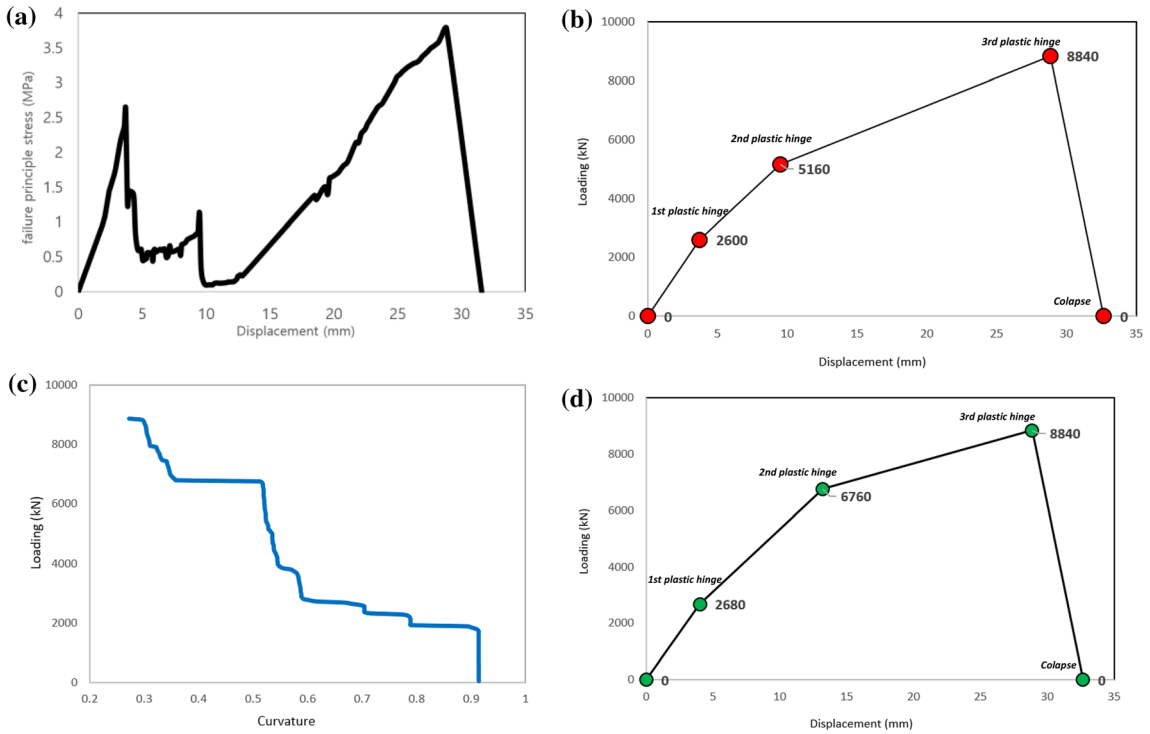

Fig. 11 Nonlinear zone (plastic hinges) deformation. **a** Variation of failure principle stress criterion versus displacement, **b** calculation of the collapse mechanism based on the first concept, **c** variation of loading versus curvature, and **d** calculation of the collapse mechanism based on the second concept

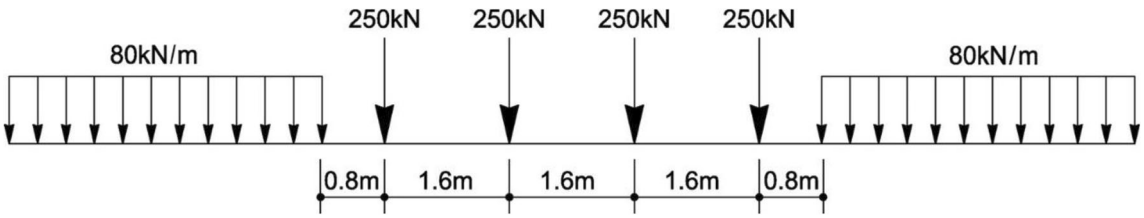

Fig. 12 Train live load on railway bridges based on UIC 776–1 for an axial load of 25-ton

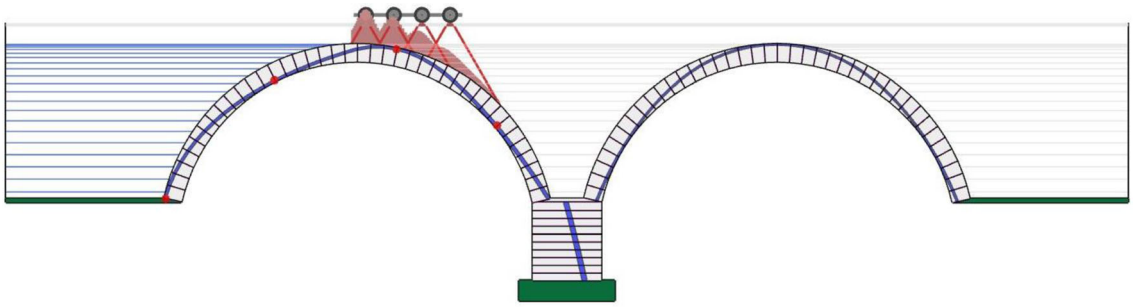

Fig. 13 Two-dimensional modeling of the Ring software based on limit state approach

position of the UIC 776–1 load distribution. The calculated factor of safety based on the limit state method is computed equal to $FS = 3.490$.

The factor of safety calculated by finite element method is 8.3% less than limit state method. The main reason for this difference is the modeling of initial cracks and comprehensiveness of the three-dimensional nonlinear finite element model. Based on the geometric properties such as span length ($l = 20$m), ring thickness ($s = 1.1$m), rise ($r = 8$m), maximum pier height ($h = 4.43$m), number of spans ($n = 2$), rise-to-span ratio ($r/l = 0.4$), and ring thickness-to-span ratio ($s/l = 0.055$), the safety factor of 50 railway masonry arch bridges is also determined as $3 \leq \text{FS} \leq 5$ [39]. Also in Ref [44] by statistical analysis and using linear elastic fracture mechanics (LEFM) theory, factors of safety was estimated about 1.8–5.4 for masonry arch bridges. Thus, the results obtained by the finite element mode are completely reliable. It is worthwhile to mention that the safety estimate provided in the present work does consider the actual damage state of the 2PL20 bridge. Finally, it may be concluded that the factor of safety for the 2PL20 bridge is 220% more than the service load for a 25-ton axial load. As a result, it can be decided that the rise of axial load up to 40% is admissible (from 25-ton up to 35-ton axial load).

6 Conclusions

There are about 3400 masonry arch bridges in Iran's railway network which most of them have been constructed more than 80 years ago. Due to the need of increasing axial loads in the current railway network, assessment of old masonry arch bridges as crucial infrastructures to obtain load-carrying capacity of them has become an important issue in the last decades. Due to the complex behavior of such bridges, accurate simulation is required to assess and study their behavior. In this study, the results from the nonlinear three-dimensional finite element modeling to evaluate the load-carrying capacity for a plain concrete arch bridge with two 20 m spans have been presented. The residual capacity of the bridge was not never determined in field test loading; therefore, the residual strength and the nonlinear response of the 2PL20 bridge are derived using the limited results obtained from filed tests and the numerical modeling. The residual strength of the bridge has been calculated equal to 8880 kN and the failure of the structure has occurred with the formation of three plastic hinges (zones) in the crown and each of the springings. The results indicate that the condition of the 2L20 bridge under 25-ton axial load with FS = 3.200 as an old railway masonry arch bridge is acceptable and it may be concluded that by considering the design safety factor equal to two, increase of axial load up to 40% (axial load of 35-ton) is allowable for railway network of Iran. In addition, the results indicate the nonlinear behavior of this structures are appropriate in post-yield stage.

Acknowledgements The authors would like to acknowledge and express their special gratitude to anonymous reviewers, for their constructive comments that improved the quality of the manuscript.

Compliance with ethical standards

Conflict of interest On behalf of all authors, the corresponding author states that there is no conflict of interest.

References

1. H. Agency, Design manual for roads and bridges, HM Stationery Office1994.
2. Wang J, Melbourne C (2010) Mechanics of MEXE method for masonry arch bridge assessment. Proc Institution Civ Eng—Eng Comput Mech 163(3):187–202
3. Gilbert M, Melbourne C (1994) Rigid-block analysis of masonry structures. Struct Eng 72(21):359–361
4. Sarhosis V, De Santis S, de Felice G (2016) A review of experimental investigations and assessment methods for masonry arch bridges. Struct Infrastruct Eng 12(11):1439–1464
5. Marefat MS, Yazdani M, Jafari M (2019) Seismic assessment of small to medium spans plain concrete arch bridges. Eur J Environ Civ Eng 23(7):894–915
6. Tubaldi E, Macorini L, Izzuddin BA (2018) Three-dimensional mesoscale modelling of multi-span masonry arch bridges subjected to scour. Eng Struct 165:486–500
7. Pulatsu B, Erdogmus E, Lourenço PB (2019) Comparison of in-plane and out-of-plane failure modes of masonry arch bridges using discontinuum analysis. Eng Struct 178:24–36
8. De Santis S, de Felice G (2014) A fibre beam-based approach for the evaluation of the seismic capacity of masonry arches. Earthquake Eng Struct Dynam 43(11):1661–1681
9. Galvín P, Romero A, Moliner E, Martínez-Rodrigo MD (2018) Two FE models to analyse the dynamic response of short span simply-supported oblique high-speed railway bridges: comparison and experimental validation. Eng Struct 167:48–64
10. Mahmoudi Moazam A, Hasani N, Yazdani M (2018) Three-dimensional modelling for seismic assessment of plain concrete arch bridges. Proc Inst Civ Eng Civ Eng 171(3):135–143
11. Choo BS, Coutie MG, Gong NG (1991) finite element analysis of masonry arch bridges using tapered elements, Proceedings—Institution of Civil Engineers. Part 2. Res Theory 91:755–770
12. Franck SA, Bretschneider N, Slowik V (2020) Safety analysis of existing masonry arch bridges by nonlinear finite element simulations. Int J Damage Mech 29(1):126–143
13. Aydin AC, Özkaya SG (2018) The finite element analysis of collapse loads of single-spanned historic masonry arch bridges (Ordu, Sarpdere Bridge). Eng Fail Anal 84:131–138
14. Fanning PJ, Boothby TE (2001) Three-dimensional modelling and full-scale testing of stone arch bridges. Comput Struct 79(29–30):2645–2662
15. Milani G, Lourenço PB (2012) 3D non-linear behavior of masonry arch bridges. Comput Struct 110–111:133–150
16. Pulatsu B, Erdogmus E, Bretas EM (2018) Parametric study on masonry arches using 2D discrete element modeling. J Architect Eng 24(2):04018005
17. Sarhosis V, Forgács T, Lemos JV (2019) A discrete approach for modelling backfill material in masonry arch bridges. Comput Struct 224:106108
18. Forgács T, Sarhosis V, Bagi K (2018) Influence of construction method on the load bearing capacity of skew masonry arches. Eng Struct 168:612–627
19. Marefat MS, Ghahremani-Gargary E, Ataei S (2004) Load test of a plain concrete arch railway bridge of 20-m span. Constr Build Mater 18(9):661–667
20. Brencich A, Sabia D (2007) Tanaro bridge: dynamic tests on a couple of spans. J Bridge Eng 12(5):662–665
21. Page J (1993) Masonry arch bridges, HM Stationery Office.
22. Casapulla C, Mousavian E, Zarghani M (2019) A digital tool to design structurally feasible semi-circular masonry arches composed of interlocking blocks. Comput Struct 221:111–126
23. Accornero F, Lacidogna G, Carpinteri A (2016) Evolutionary fracture analysis of masonry arches: Effects of shallowness ratio and size scale. Comptes Rendus Mécanique 344(9):623–630
24. Yazdani M, Azimi P (2020) Assessment of railway plain concrete arch bridges subjected to high-speed trains. Structures 27:174–193
25. Severini L, Cavalagli N, DeJong M, Gusella V (2018) Dynamic response of masonry arch with geometrical irregularities subjected to a pulse-type ground motion. Nonlinear Dyn 91(1):609–624
26. Forgács T, Sarhosis V, Ádány S (2021) Shakedown and dynamic behaviour of masonry arch railway bridges. Eng Struct 228:111474
27. Mahmoudi Moazam A, Hasani N, Yazdani M (2018) Incremental dynamic analysis of small to medium spans plain concrete arch bridges. Eng Fail Anal 91:12–27
28. Homaei F, Yazdani M (2020) The probabilistic seismic assessment of aged concrete arch bridges: The role of soil-structure interaction. Structures 28:894–904
29. Jahangiri V, Yazdani M (2021) Seismic reliability and limit state risk evaluation of plain concrete arch bridges. Struct Infrastruct Eng 17(2):170–190
30. Conde B, Eguía P, Stavroulakis GE, Granada E (2018) Parameter identification for damaged condition investigation on masonry arch bridges using a Bayesian approach. Eng Struct 172:275–284
31. Moazam AM, Hasani N, Yazdani M (2017) 3D simulation of railway bridges for estimating fundamental frequency using geometrical and mechanical properties. Adv Comput Design 2(4):257–271
32. Yazdani M, Khaji N, Khodakarami MI (2016) Development of a new semi-analytical method in fracture mechanics problems based on the energy release rate. Acta Mech 227(12):3529–3547
33. Yazdani M, Khaji N (2018) Development of a new semianalytical approach for 2D analysis of crack propagation problems. Fatigue Fract Eng Mater Struct 41(6):1344–1363
34. Khoei A, Yasbolaghi R, Biabanaki S (2015) A polygonal finite element method for modeling crack propagation with minimum remeshing. Int J Fract 194(2):123–148
35. Wang G, Wang Y, Lu W, Zhou C, Chen M, Yan P (2015) XFEM based seismic potential failure mode analysis of concrete gravity dam–water–foundation systems through incremental dynamic analysis. Eng Struct 98:81–94
36. Willam KJ (1975) Constitutive model for the triaxial behaviour of concrete. Proc Intl Assoc Bridge Structl Engrs 19:1–30
37. A. Committee, I.O.f. Standardization, Building code requirements for structural concrete (ACI 318–08) and commentary, American Concrete Institute, 2008.
38. Fanning P, Kelly O (2000) Smeared crack models of RC beams with externally bonded CFRP plates. Comput Mech 26(4):325–332
39. De Santis S, de Felice G (2014) Overview of railway masonry bridges with a safety factor estimate. Int J Architect Heritage 8(3):452–474
40. Melbourne C, Tomor AK, Wang J (2004) Cyclic load capacity and endurance limit of multi-ring masonry arches, In: Arch bridges IV conference proceedings, pp 375–384.

41. Sotoudeh S, Jahangiri M, Ranjbarnia M, Zakeri J-A (2020) Three-dimensional modeling of an old masonry bridge and assessing its current capacity. Periodica Polytechnica Civ Eng 64(2):460–473
42. U. Code, 776-1, Loads to be considered in railway bridge design, International Union of Railway, 2006
43. U. Code, 778-3, 2011, Recommendations for the inspection, assessment and maintenance of masonry arch bridges.
44. Panian R, Yazdani M (2020) Estimation of the service load capacity of plain concrete arch bridges using a novel approach: stress intensity factor, Structures, Elsevier pp 1521–1534